FLEXIBLE COMPOSITE WING WITH INTERNAL ACTUATION FOR ROLL MANEUVER

N. S. Khot, J. V. Zweber and D. E. Veley
Air Force Research Laboratory (AFRL/VASD)

H. Öz
Ohio State University, Department of Aerospace Engineering and Aviation

F. E. Eastep
University of Dayton, Department of Mechanical & Aerospace Engineering

Keywords: *composite material, flexible wing, control design, roll maneuver, smart structures*

Abstract

This paper is concerned with designing an optimum composite flexible wing structure to enhance roll maneuver capability at high dynamic pressures using an embedded actuating system without external control surfaces. A minimum weight design, with constraints on strength for three different flight conditions, on the frequency distribution and lift effectiveness was used for this study. The elastic twist and camber is achieved by providing a system of actuating elements distributed within the internal substructure of the wing to provide control forces. The modal approach is used to develop the dynamic equilibrium equations which culminates in the steady roll maneuver of a wing subjected to aerodynamic loads and the actuating forces. The distribution of actuating forces to achieve the specified steady roll rate and roll angle of the flexible vehicle within a specified time was determined by using Independent Modal-Space Control (IMSC) design approach. Here, a full-scale realistic wing is considered for the assessment of the strain energy and distribution of actuator forces required to produce the antisymmetric twist and camber deformation to achieve the specified roll performance.

1 Introduction

Traditionally, a pilot provides a rolling maneuver for turning of the aircraft with an aileron system by rotation of trailing edge control surfaces on the right and left wings in a differential sense. The aileron system increases the lift on one wing and decreases lift on the opposite wing resulting in a rolling moment producing the rolling maneuver. This is an effective technique for generating rolling moment for an aircraft operating in a low dynamic pressure environment where the wings are essentially “rigid”. However, if the aircraft is operating at high dynamic pressures where the deformations of the wings are significant, the roll rate is reduced by a detrimental aerodynamic twisting moment resulting from the trailing edge control surface rotation. At roll reversal dynamic pressure the ailerons are rendered completely ineffective for producing the needed rolling moment. Reference [1] describes a technique for prescribing elastic wing twist and camber distribution for the enhancement of the rolling maneuver of a wing at all dynamic pressures without ailerons. The control forces were obtained from a technique referred to as “Fictitious Control Surfaces”. In Reference [2] an optimized structure was designed to achieve a specified roll rate without ailerons at different Mach numbers by using a static aeroelastic approach. Rather than using an aileron system to achieve an aerodynamic rolling moment, here wing deformation is used as an asset rather than impediment to overcome, which avoids the detrimental twisting moment of the aileron and enhances the roll performance at all dynamic pressures. The wing is twisted and cambered in a differential sense on the right

and left wings as shown in Figure 1, to achieve the required rolling moment for a specified steady roll rate.

Presently, there are DARPA sponsored projects [3] for demonstration of the application of smart materials for twist control to improve aircraft performance based solely on test results from small wind-tunnel models. Here, it is proposed that a full scale finite element model of a realistic wing be considered for proper elastic wing twist and camber for roll control in a high dynamic pressure environment. The approach selected here is a two step process. In the first step, an optimum structural design satisfying requirements on strength, frequency distribution and lift effectiveness is obtained. The optimization problem was solved by using ASTROS [4] version 20 for three flight condition at 9-g symmetric pull-up maneuver at M=0.85. In the second step the axial load carrying cross rod elements mounted to the internal structure are used as actuators exerting tensile /compressive loads to twist and camber the optimum wing structure via an active control strategy to achieve specified roll rates and roll angles. The control design approach is based on using Independent Modal-Space Control (IMSC) [5]. The present paper contains a short summary of this approach as applied to the roll maneuver of a flexible aircraft.

2 ANALYTICAL APPROACH

2.1 Modal Dynamic Equilibrium Equations

The dynamic equilibrium equations for steady roll maneuver can be written as [2], [6]

$$[M]\{\ddot{r}_s\} + [C]\{\dot{r}_s\} + [K]\{r_s\} + q_d[T]^T[A]\{\alpha\} + [F]\{\bar{u}(t)\} = 0 \quad (1)$$

where $[M]$ is the mass matrix, $[C]$ is the damping matrix, $[K]$ is the structural stiffness matrix of the finite element model, $\{r_s\}$ is the vector of nodal displacements, q_d is the dynamic pressure, [T] is the transformation matrix from structural degrees of freedom to the aerodynamic degrees of freedom, $\{\alpha\}$ is the vector of angles of attack at the aerodynamic panels, $[F]$ is the applied actuator load distribution matrix and $\{\bar{u}(t)\}$ is the vector of actuator stimuli which is a function of time t. The product $[F]\{\bar{u}(t)\}$ is the vector of generated control forces generated at the structural node points due to the actuator forces $\{\bar{u}(t)\}$ or due to the voltages applied to the solid state actuators. In the latter case the elements of matrix $[F]$ would depend on the number of stacks, number of cycles and the properties of the solid state actuators in addition to the direction cosines associated with the actuators.

The displacement vector $\{r_s\}$ can be defined as a linear combination of rigid body modes and elastic vibration modes as

$$\{r_s\} = [\Psi_r]\{q_r\} + [\Psi_e]\{q_e\} = [\psi]\{q\} \quad (2)$$

where $[\Psi_r]$ is the rigid body mode, $[\psi_e]$ is the specified number of antisymmetric low frequency modes, $\{q_r\}$ is the generalized rigid body displacements and in present case it is equal to the roll angle ϕ. In Equation (2) $\{q_e\}$ represents the elastic displacements. The subscripts *r* and *e* are used to indicate rigid body and flexible vibration modes.

The angles of attack $\{\alpha\}$ at the control points of aerodynamic panels can be written as

$$\{\alpha\} = \frac{1}{V}[T]\{\dot{r}_s\} \quad (3)$$

where V is the free stream velocity. Using Equation (2) the angles of attack can be written as

$$\{\alpha\} = \frac{1}{V}[T]\left[[\Psi_r]\{\dot{q}_r\} + U\left[\frac{\partial\psi_e}{\partial\bar{x}}\right]\{q_e\}\right] \quad (4)$$

where $\dot{q}_r$ is the roll rate Z^*, U is the chord wise component of V in the direction $\bar{x}$, $[(\partial\psi_e)/(\partial\bar{x})]$ is the matrix of flexible mode gradients with respect to the $\bar{x}$ coordinate. Equation (4) can be written as

$$[\alpha] = \left[\frac{\bar{\Psi}_r}{V}\ \frac{\partial\bar{\psi}_e}{\partial q_e}\right]\begin{Bmatrix}\dot{q}_r\\ q_e\end{Bmatrix} \quad (5)$$

where $\bar{\Psi}_r = T\Psi_r$ and $\bar{\Psi}_e = T\Psi_e$ are the rigid and vibration modes expressed in aerodynamic degrees of freedom. Using Equation (5) the equilibrium Equation (1) can be written in terms of generalized coordinates as

$$[M_s]\{\ddot{q}\} + [C_a]\{\dot{q}\} + [K_{sa}]\{q\} = \{Q\} \quad (6)$$

$$\text{where } [M_s] = [\Psi]^T[M][\Psi] \quad (7)$$

$$[C_a] = q_d[\bar{A}_c],\ [K_a] = q_d[\bar{A}_k] \quad (8)$$

$$[K_{sa}] = [\bar{K}_s] + [K_a] \quad (9)$$

$$[\bar{K}_s] = \begin{bmatrix} 0 & 0 \\ 0 & [\Psi]^T[K][\Psi] \end{bmatrix} \quad (10)$$

$$[\bar{A}] = [\Psi]^T[T]^T[A] = [\bar{A}_c] + [\bar{A}_k] \quad (11)$$

$$\{Q\} = -[\Psi]^T[F]\{\bar{u}(t)\} \quad (12)$$

in which $[M_s]$ and $[\bar{K}_s]$ are the modal structural mass and stiffness matrices respectively; $[C_a]$ and $[K_a]$ are the modal aerodynamic damping and aerodynamic stiffness matrices, respectively; $[K_{sa}]$ is the modal aeroelastic stiffness matrix. In Equation (11) the aerodynamic damping matrix $[\bar{A}_c]$ is obtained from $[\bar{A}]$ with all elements set to zero except the first column and $[\bar{A}_k]$ is obtained from $[\bar{A}]$ with first column elements set to zero. Equation (6) represents the aeroelastic roll dynamics equations of motion in the configuration space represented by the generalized coordinates which are the structural modal coordinates and $\{Q\}$ represents the generalized control loads in the same configuration space.

2.2 Independent Modal -Space Control Design of Aeroelastic System

The state space equations corresponding to Equation (6) can be written as[5]

$$\begin{bmatrix} M_s & 0 \\ 0 & M_s \end{bmatrix}\begin{bmatrix} \ddot{q} \\ \dot{q} \end{bmatrix} + \begin{bmatrix} C_a & K_{sa} \\ -M_s & 0 \end{bmatrix}\begin{bmatrix} \dot{q} \\ q \end{bmatrix} = \begin{bmatrix} Q \\ 0 \end{bmatrix} \quad (13)$$

Equation (13) can be written as

$$M\dot{x} + Gx = X \quad (14)$$

where M, G and X represent corresponding matrices in Equation (13) and x is the state vector.

Introducing the general solution form $x = v_r e_r^{\lambda t}$ into the homogeneous form of Equation (14) the right (R) and left (L) conjugate aeroelastic eigenvalue problems can be posed as

$$[\lambda_r M + G]V_{Rr} = 0,\ [\lambda_r M^T + G^T]V_{Lr} = 0 \quad (15)$$

where V_{Rr} and V_{Lr} are the right and left aeroelastic eigenvectors, respectively, corresponding to the r-th aeroelastic eigenvalue λ_r. Once the complex general conjugate eigenvalue problems are solved, one no longer needs to deal with complex quantities and the problem can be dealt with in terms of real modal matrices and real modal-state variables formed from the real and imaginary parts of the right and left eigenvectors and the complex modal state. The resulting real aeroelastic modal state transformation and the bi-orthonormality relationships for the aeroelastic real modal matrices are

$$V_L^T M V_R = I,\ V_L^T G V_R = \text{block-diag}[\Delta_r] \quad (16)$$

$$[\Delta_r] = \begin{bmatrix} \alpha_{r1} & \omega_r \\ -\omega_r & \alpha_{r2} \end{bmatrix} \quad (17)$$

$$\alpha_{r1,\,r2} = Re\lambda_{r1,\,r2} \qquad \omega_r = Im\lambda_{r1,\,r2} \quad (18)$$

$$x(t) = V_R w(t) \quad (19)$$

$$w = [w_1, w_2, \ldots w_r, \ldots w_n]^T \quad (20)$$

$$w_r = \left[\xi_r(t)\ \eta_r(t)\right]^T \quad (21)$$

where V_L and V_R are the real conjugate left and right aeroelastic modal matrices, respectively. In Equation (20), w is the $n_s = 2n$ vector of aeroelastic modal-states, ξ_r and η_r (r=1,2,.....n) are a conjugate pair of the r-th real modal-states. In the above equations $r1$ and $r2$ denote the r-th pair of eigenvalues. The uncoupled aeroelastic modal-state-space equations for designing the

control system can be obtained by utilizing the solution of the eigenvalue problem given in Equations (15-21) and the generalized configuration-space input Q.This approach is known as Independent Modal Space Control (IMSC). One now is free to use his favorite control theory to design the single modal control input for each uncoupled pair of modal-state equations. In this paper, LQR control design approach is used to design the uncoupled set of state equations. The coupling terms arising through the constraint equations are in general very weak and therefore have virtually a null effect on the system.

The objective function for minimization selected here in order to determine the contribution z_r^* of different aeroelastic modes to achieve the desired roll rate Z^* is the elastic strain energy to achieve the specified roll rate.The work-energy equation is obtained by taking the scaler product of the vector form of Equation (6) with the incremental generalized coordinate displacement vector $dq(t)$ and integrating between specified time interval during the maneuver. Thus denoting by the work terms due to acceleration loads (kinetic energy), elastic loads, aerodynamic damping and aerodynamic stiffness loads, and actuator loads, respectively, the energy equilibrium equation can be written as:

$$W_{kin} + W_{flx} + W_{ard} + W_{ars} = W_{act} \qquad (22)$$

3 Aeroelastic Analysis

The Unified Subsonic and Supersonic Aerodynamic Analysis (USSAERO) [7] was used for the computation of aerodynamic loads on the aircraft wing. This approach uses a superposition of vortex singularities applied to a discrete number of aerodynamic panels to calculate the discrete pressure distribution over the wing surface. In this investigation numerical calculations for rigid and flexible vibration modes, aerodynamic stability derivatives, generalized stiffness matrix etc. are calculated from ASTROS [4]. The special version of ASTROS was run with bulk data containing the location and description of the actuators. In the present case the actuators were assumed to be rod elements capable of exerting only axial loads. The required data for solution of the approach discussed in the last section were written on separate files after execution of the ASTROS run. Separate program was written to obtain the generalized matrices defined in Equations (7) through (12) from the matrices calculated by ASTROS and the IMSC control design program was written using MATLAB language to calculate the distribution of actuator forces, time response of the roll rate, work-energy quantities etc.

4 Numerical Examples

A low aspect ratio wing was selected for this study. The wing planform is shown in Figure 2 along with the location of the underlying structure. The wing planform was divided into 180 aerodynamic boxes. Figure 3 shows the underlying structure, consisting of 10 intermediate spars and 6 intermediate ribs, represented with finite elements. The wing structure was idealized using 167 nodes and was modeled using graphite-epoxy wing skins and aluminum substructure. The wing skins were modeled as 40 quadrilateral and seven triangular elements per side with a (90, 0, -45, 45) symmetric laminate on each element. The 0 degree direction is defined to be parallel to the y-axis of the aircraft coordinate system. The wing substructure was modeled as 105 quadrilateral “picture frame” elements. Each quadrilateral rib or spar element was built as a shear element to represent the web bounded by bar elements on the top and bottom to model caps and rod elements on the sides, “posts”, to model the additional material needed for spar to rib connections. In addition to the load-bearing wing structure, appropriate single and multi-point constraints and structure were specified for simulation of the wing carry-through structure and an 8000 lbs. mass was used to simulate the weight of the fuselage. Finally, 1600 lbs. of non-structural mass were distributed amongst different node points on the wing to simulate fuel, plumbing, wiring and fastener weights.

The model was initially sized to obtain the minimum weight structure that would satisfy a

number of constraints. During this design, the thicknesses of the 90, 0 and ±45 degree layers of the skin were allowed to vary individually as well as the thicknesses of the shear elements and the cross sectional areas of the bar and rod elements in the picture frame elements. This resulted in a total of 656 design variables: 282 skin variables (47 elements x 2 surfaces x 3 layers) and 374 substructure variables (105 shear panels + 210 bar elements + 59 rod elements). The constraints on the optimization were that the stresses in the elements being resized did not exceed their allowables at three different flight conditions. The stress constraints were formulated as Tsai-Wu for the composite elements and Von Mises for the metallic elements. Additional constraints were imposed to limit the frequency of the first flexible mode was 3 Hz and the lift effectiveness to at least 0.9 at one flight condition. The lift effectiveness constraint, flexible lift curve slope divided by rigid lift curve slope, was applied at Mach 0.85 at sea level on a standard day.

The flight conditions chosen for the stress constraints were a dynamic 9-g pull-up at Mach 0.85 at a dynamic pressure of 30 psi and steady (zero pitch rate) 9-g pull-ups at Mach 0.85 and dynamic pressures of 15 and 7.43 psi. The 7.43 psi case represents match point conditions for sea level on a standard day. The other two conditions were chosen to provide different loading conditions. The reason for these different loading conditions can be seen by examining the static aeroelastic problem formulation:

$$[\boldsymbol{K} - \boldsymbol{AICS}(q_d, M)]u + \boldsymbol{M}\ddot{u} = \boldsymbol{P}(q_d, M)\delta \quad (23)$$

where, $\boldsymbol{P}(q_d, M) = q_d[\boldsymbol{G}]^T[\boldsymbol{AIRFRC}(M)]$ (24)

and $\boldsymbol{AICS}(q_d, M) = q_d[\boldsymbol{G}]^T[\boldsymbol{AIC}(M)][\boldsymbol{G}]$ (25)

For a rigid wing, $[\boldsymbol{AICS}] = [\boldsymbol{AIC}] = 0$, a change in dynamic pressure merely results in a scaling of the force term, $[\boldsymbol{P}]$, as can be seen from Equation (24). However, for the case of a flexible wing, the dynamic pressure effect in both the non-zero $[\boldsymbol{AICS}]$ term, shown in Equation (25), and the force term result in a changing load distribution as the dynamic pressure is varied.

The results of the optimization where that the structural mass of the wing was reduced from 2353 lbs. to 345 lbs. This optimized weight is reasonable for a 20,000 lbs. fighter. It results in a wing weight fraction of about 3.5%. Plots of the thickness distribution of the wing skins are shown in Figures 4, 5 and 6 for the 0, 90 and ±45 degree layers respectively. As expected, most of the thickness was retained in the 0 degree layer near the root. This location is where the material and fiber orientation can most effectively carry the bending load of the wing. In addition, it can be seen that moderate thickness is retained in all layers near the wing tip. This is likely due to the lift effectiveness constraint. By stiffening the wing tip, the wing is able to withstand the aerodynamic twisting moment that will otherwise degrade the lift performance of the wing.

The stiffening of the wing tip can also be seen in Figure 7. This figure shows the thicknesses of the shear elements of the spar and rib picture frame elements. In this figure, the thickest elements are in the two outer most rib. These elements are the most effective shear elements in countering a local torsion of the wing.

The final set of structural design variables were the spar and rib cap and post cross-sectional areas. The results for these elements are Figure 8. It can be seen that three spar cap elements at the trailing edge root of the wing are significantly larger than any of the other cap or post elements. This is most likely the result of a path dependency in the optimization. One possible change that could be investigated is modeling the spar and rib caps as rod elements instead of bar elements. The areas of the three largest cap elements were omitted from Figure 9 in order to show the relative sizes of the remaining elements. Figure 9 reinforces the conclusions that were presented above. Again, significant stiffness was added to the tip of the wing.

The actuating system to twist and camber the wing consisted of 40 cross rods along the five ribs as shown in Figure 3. Actuators were of a generic nature capable of providing tensile or compressive forces as required to deform the wing to achieve the specified flexible roll rate. The required total strain energy and the magni-

tude of forces necessary to twist the wing to achieve specified flexible roll rate at Mach numbers 0.85 and 1.2 were calculated. The target flexible roll rate was specified as 90^o /sec at an altitude of 20,000 ft.

The controller was designed by using six aeroelastic modes of the servoelastic modal state equation.The LQR control design approach was used to design the single modal control input for each uncoupled pair of modal-state dynamics. In the definition of the LQR performance index for each aeroelastic mode the state weighting matrix was assumed to be diagonal and the control weighting matrix was a scalar. The elements of the state weighting matrix were set equal to unity. However, each modal control weighting matrix r_w was assumed to be the same for all the modes. Different values r_w were used to investigate its effect on the time response and the magnitude of the actuator forces. As the evaluation model, first twenty flexible structural modes were used in addition to the rigid body roll mode as defined by Equations (2) and (13). The results and the work done by the actuators given in the paper are for the evaluation model even though the control design is based on the reduced-order aeroelastic modal model. The time response for the reduced order controller (6 aeroelastic modes) and the evaluation model (21 structural modes) was not much different indicating negligible spillover effect. The individual contribution of different modes to achieve 90 deg/sec roll rate was determined by using the modal performance allocation optimization approach in order to minimize the total flexible strain energy due to the work done by the actuators and aerodynamic loads. For Mach number 0.85 the percentage allocation amongst six aeroelastic modes 1 through 6 was 0.0, 42.0, 30.0, 29.0, -0.3, -0.7, respectively. For Mach number 1.2 the percentage allocation amongst the six modes was 0.0, 87.1, 205.1, -197.0, 19.5, -14.7 respectively. The time response and the energy quantities were calculated for a period of four seconds.

Table 1 gives the actuator work associated with the flexible modal coordinates of the evaluation model for the two Mach numbers 0.85 and 1.2 for the control weighting parameter $r_w = 0.1$, 1.0 and 10.0, respectively. The actuator work was equal to the total energy satisfying equilibrium Equation 22. The decrease in the total energy requirement at high Mach number is due to the increase in the lift-pressure helping to create the required rolling moment. Comparing the actuator work it is observed that it increases with increase in the value of the control weighting parameter r_w. For example at MACH=1.2, the flexible wing needed 2673 in-lbs and 3413 in-lbs to achieve the roll rate of 90^o /sec for the control weighting parameter $r_w = 0.1$ and 10.0 respectively. Table 2 shows the distribution of open-loop and closed-loop eigenvalues for the two Mach numbers. For both cases first four flexible modes are unstable having positive real parts of the open-loop eigenvalues.The closed loop systems are stable. Figure 10 shows the aeroelastic deformation of the wing for Mach number 0.85. The wing twist and bending provides positive angle of attack at most of the locations.The maximum displacements at the trailing edge of the tip of the wing were different for the two Mach numbers. However, the general deformation patterns were similar. The maximum deflection for Mach 0.85 and 1.2 was 1.51 in and 1.14 in, respectively. High dynamic pressure required smaller deformation than the lower dynamic pressure.The time history for the roll rate and the actuator forces for Mach 0.85 and 1.2 for $r_w = 0.1$ and 10.0 are shown in Figures 11 through 18. In these figures in addition to the roll rate, roll angle is also shown as a function of time.

The response plots for roll rate and the actuator forces for different values of the control parameter are shown side by side in order to indicate the relationship between the time required to stabilize the roll rate at the desired value and the magnitude of the actuator forces. For smaller values of $r_w = 0.1$ the roll rate tend to stabilize faster but the magnitude of the actuator forces increases. For $r_w = 10.0$ the roll rate does not yet stabilize closer to 90 deg/sec even after 4 sec, but the magnitude of maximum forces is very close to 2000 lbs. This is a substantial reduction in the required magnitude of the forces, but at the expense of roll rate settling

time. It is interesting to note that even though the roll rate tend to stabilize at different times the roll angle is increased nearly at the rate of 90 deg/sec throughout the maneuver. This is due to the average roll rate being nearly equal to 90 deg/sec during most of the period. For all the cases presented the roll angle increased from 0 deg. at time t =0.0 sec to 360 deg. at t_f = 4.0 sec. If achieving required roll angle is more important than stabilizing the roll rate, these results show that it can be achieved with lesser magnitude of the control forces within the required time with higher magnitude of actuator work.(see Table 1)

5 Conclusions

In this investigation, the flexibility of a wing is used as a departure away from the traditional aileron system, which results in a detrimental aerodynamic twisting moment and possibly in unacceptable roll performance at high dynamic pressures. A realistic composite wing was optimized with constraints on the strength, frequency distribution and lift effectiveness to obtain a feasible flexible wing structure. Rather than using the traditional aileron, we have investigated the use of elastic twist and camber of the whole wing to achieve acceptable roll performance at all dynamic pressures via an active control approach.

A modal-based analytical approach was used to write the dynamic equilibrium equations to achieve a steady roll maneuver and the Independent Modal-Space Control Technique was utilized to determine the distribution of actuator forces. The work done by the actuators was calculated at different Mach numbers and control weighting parameters to assess the energy requirements and the magnitude of actuator forces. The actuating system consisted of rods along the ribs, which were assumed to be of generic nature, capable of exerting tensile or compressive forces as required. The strain energy requirement decreased with increase in dynamic pressure or Mach number. The increase in the control weighting parameter increased the time required to stabilize the roll rate, however the maximum magnitude of the actuator forces decreased. Even though the roll rate stabilized to the specified magnitude at different times the roll angle increased gradually with time. If achieving a desired roll angle within specified time is important and not the roll rate than it can be attained with less magnitude of control forces. In the near future, it is anticipated that elastic twist, adding camber and providing necessary stiffness to prevent flutter and local buckling can be achieved through the use of future “smart” materials and actuating system.

6 REFERENCES

[1] Khot, N. S., Eastep, F. E. and Kolonay, R. M. “Wing twist and Camber for the Rolling Maneuver of a Flexible Wing without Ailerons”, AIAA-97-1268 Presented at 38th AIAA/ASME/ASCE/AHS/ Adaptive Structures Forum, Kissimmee, Fl. April. 1997.

[2] Khot, N. S., Appa, K. and Eastep, F. E., “Optimization of a Flexible Wing without Ailerons for the Rolling Maneuver”, To be Published in the Journal Of Aircraft, 2000.

[3] Kudva, J., Appa, K., Martin, C., Sendeckyj, G., and Harris, T., “Design, Fabrication and Testing of the DARPA/WL ‘Smart Wing’ Wind Tunnel Model” AIAA-97-1198, Presented at 38th AIAA/ASME/ ASCE/AHS/ Adaptive Structures Forum, Kissimmee, Fl. April. 1997 SPIE

[4] ASTROS User’s Reference Manual for Version 20, Universal Analytics, Inc. torrance Ca.

[5] Öz, H., “Aeroservoelastic Design with Distributed Actuation for High Performance Aircraft”, 5th SPIE Smart Structures Conference, Mathematics and Control in Smart Structures, Vol. 3323, 1998.

[6] Appa, K., Ausman, J. and Khot, N. S., “Feasibility Assessment and Optimization Study of Smart Actuation Systems for Enhanced Aircraft Maneuver Performance” WL-TR-97-3083, July,1997.

[7] Woodward, F. A., “An Improved Method for the Aerodynamic Analysis of Wing - Body- Tail Configurations in Subsonic and Supersonic Flow”, Part I -theory and Application NASA CR-2228, May 1973.

Table 1: Actuator work (in lab) from the flexible modal coordinates to achieve 90 deg/sec roll rate (altitude 20,000 ft)

Control Weighting Parameter rw	Mach 0.85	Mach 1.20
0.1	2712	2673
1.0	3211	3093
10.0	3805	3413

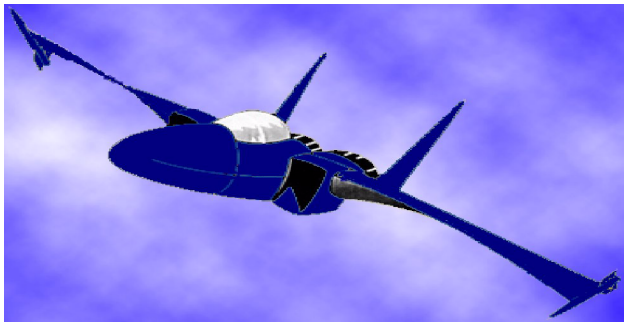

Figure 1.Flexible wing

Table 2: Aeroelastic eigenvalues

		Mode No.	real	imaginary
Mach 0.85	open loop	2	4.1604×10^{-4}	$\pm 3.8776 \times 10^{1}$
		3	1.7776×10^{-3}	$\pm 9.6986 \times 10^{1}$
		4	2.8561×10^{-3}	$\pm 1.3232 \times 10^{2}$
		5	2.5933×10^{-5}	$\pm 1.5679 \times 10^{2}$
		6	-1.0297×10^{-4}	$\pm 1.9582 \times 10^{2}$
	closed loop	2	-1.6907×10^{-1}	$\pm 3.8776 \times 10^{1}$
		3	-7.1996×10^{-1}	$\pm 9.686 \times 10^{1}$
		4	-9.3953×10^{-1}	$\pm 1.3232 \times 10^{2}$
		5	-1.2060×10^{1}	$\pm 1.5679 \times 10^{2}$
		6	-4.3888×10^{-1}	$\pm 1.9582 \times 10^{2}$
Mach 1.20	open loop	2	2.7882×10^{-4}	$\pm 4.1934 \times 10^{1}$
		3	4.8244×10^{-4}	$\pm 1.0166 \times 10^{2}$
		4	2.4886×10^{-3}	$\pm 1.3946 \times 10^{2}$
		5	3.5249×10^{-5}	$\pm 1.5687 \times 10^{2}$
		6	-1.7083×10^{-4}	$\pm 1.9621 \times 10^{2}$
	closed loop	2	-7.7800×10^{-1}	$\pm 4.1942 \times 10^{1}$
		3	-9.3464×10^{-1}	$\pm 1.0166 \times 10^{2}$
		4	-17028×10^{0}	$\pm 1.3946 \times 10^{2}$
		5	-2.5423×10^{-1}	$\pm 1.5687 \times 10^{2}$
		6	-2.3584×10^{-1}	$\pm 1.9621 \times 10^{2}$

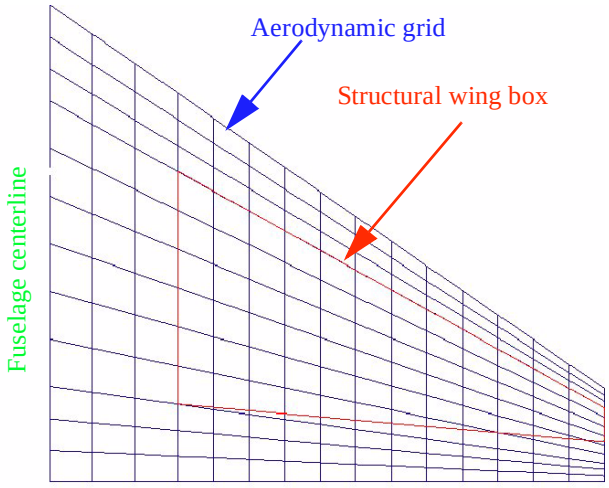

Figure 2.Aerodynamic grid

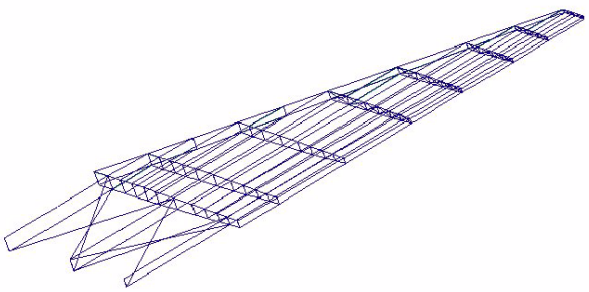

Figure 3.Finite Element Model

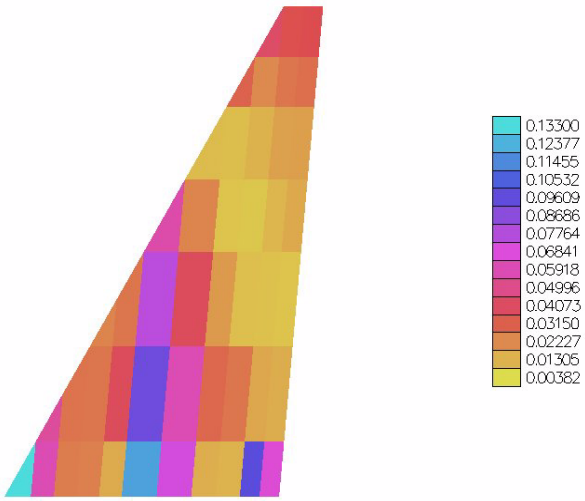

Figure 4.Bottom Skin 0 degree Ply Thicknesses

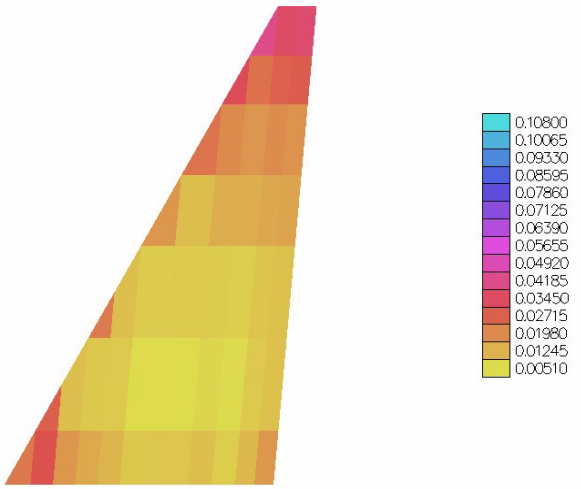

Figure 5.Bottom Skin 90 degree Ply Thicknesses

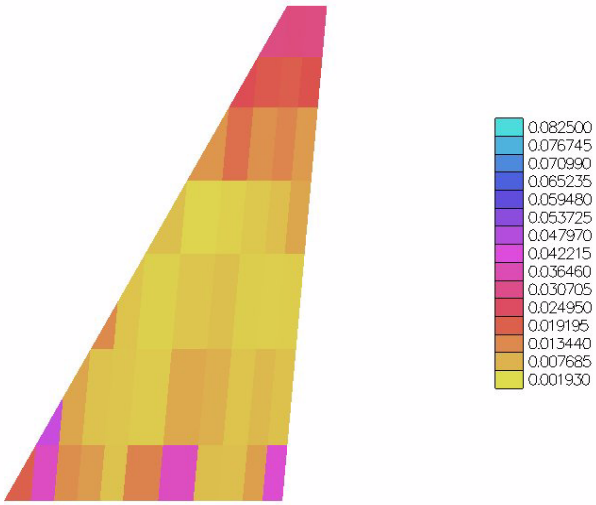

Figure 6.Bottom Skin ±45 degree Ply Thicknesses

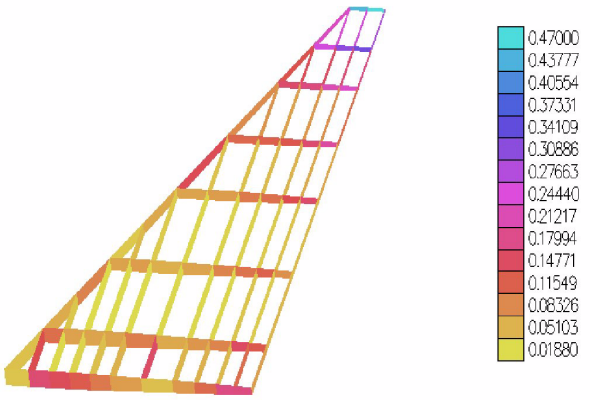

Figure 7.Spar and Rib Shear Element Thicknesses

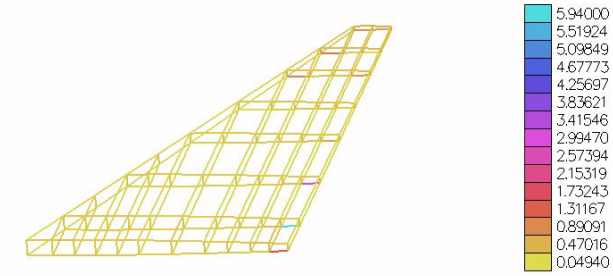

Figure 8.All Spar and Rib Cap and Post Element Cross-Sectional Areas

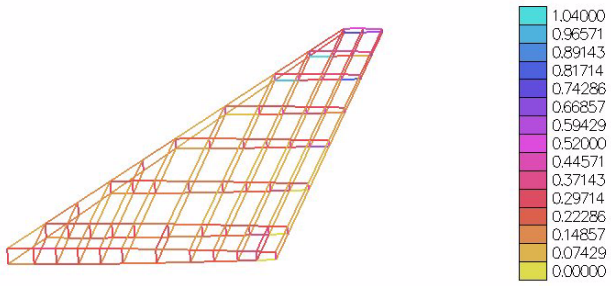

Figure 9.Selected Spar and Rib Cap and Post Element Cross-Sectional Areas

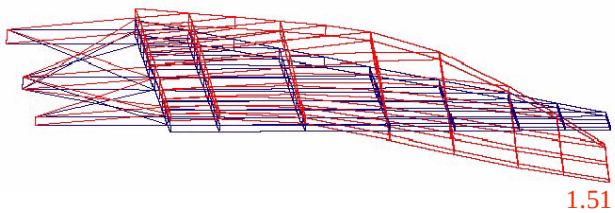

Figure 10.Mach 0.85 deformation

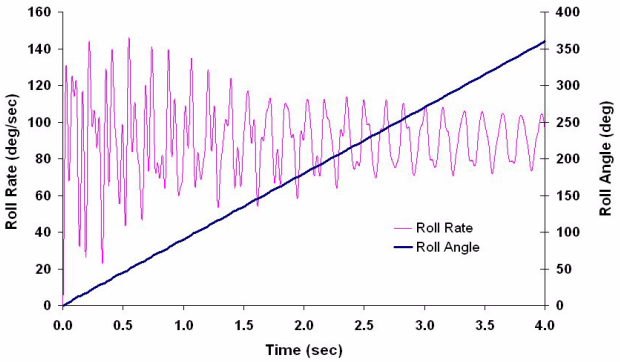

Figure 11.Time history of the roll rate and roll angle, M=0.85, control weighting parameter = 0.1

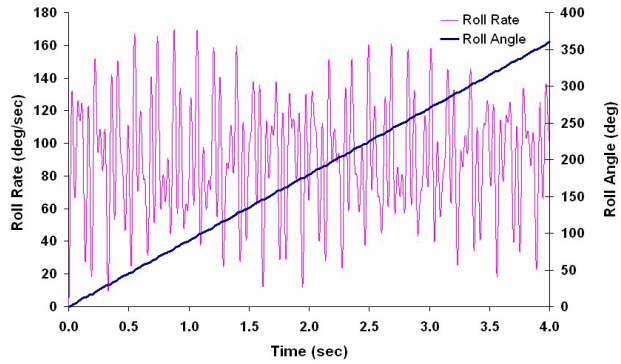

Figure 12.Time history of the roll rate and roll angle, M=0.85, control weighting parameter = 10.0

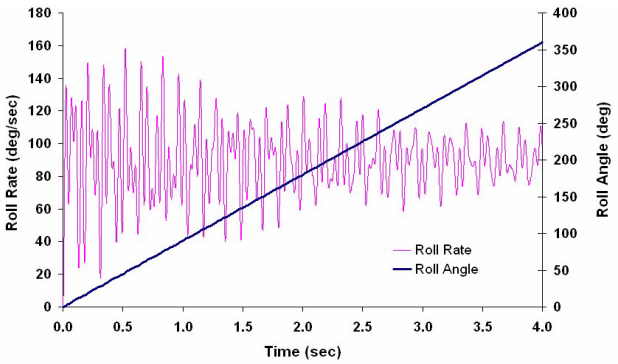

Figure 13.Time history of the roll rate and roll angle, M=1.20, control weighting parameter = 0.1

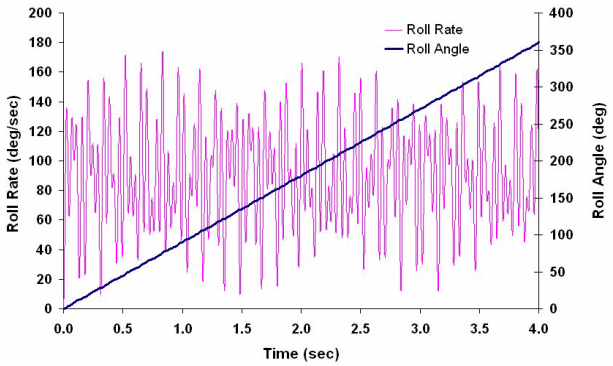

Figure 14.Time history of the roll rate and roll angle, M=1.20, control weighting parameter = 10.0

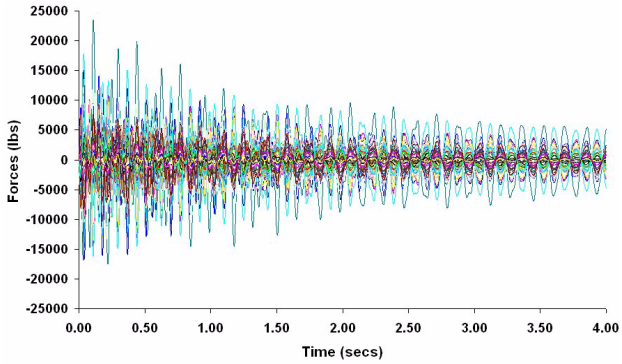

Figure 15.Time history of the actuator forces at M=0.85, control weighting parameter = 0.1

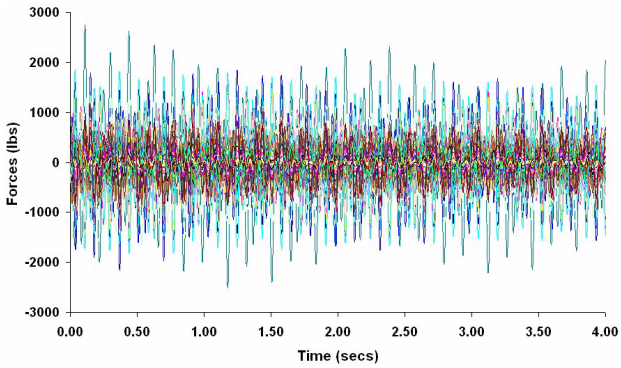

Figure 16.Time history of the actuator forces at M=0.85, control weighting parameter = 10.0

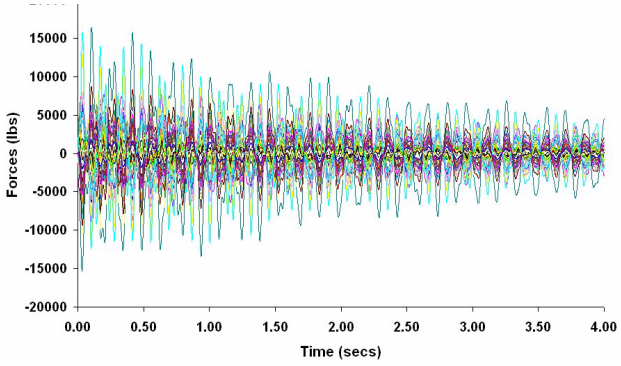

Figure 17.Time history of the actuator forces at M=1.20, control weighting parameter = 0.1

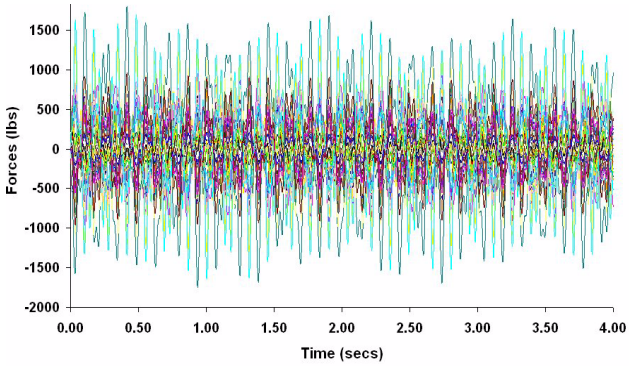

Figure 18.Time history of the actuator forces at M=1.20, control weighting parameter = 10.0